The Astrophysical Journal, 1004:86 (9pp), 2026 June 10 https://doi.org/10.3847/1538-4357/ae6f09

Observations of Circularly Polarized Radio Emission from the "Quiet" Sun at Frequencies <100 MHz

Shaik Sayuf[1], C. Kathiravan[1], R. Ramesh[1], Indrajit V. Barve[2], G. V. S. Gireesh[2], and Kshitij S. Bane[3]
[1] Indian Institute of Astrophysics, Koramangala 2nd Block, Bangalore 560034, Karnataka, India; shaik.sayuf@iiap.res.in
[2] Radio Astronomy Field Station, Indian Institute of Astrophysics, Gauribidanur 561210, Karnataka, India
[3] National Centre for Radio Astrophysics, Tata Institute of Fundamental Research, Pune 411007, Maharashtra, India
Received 2025 December 24; revised 2026 May 12; accepted 2026 May 15; published 2026 June 8

Abstract

The presence of the magnetic field makes the solar coronal medium birefringent. Research indicates that an appreciable degree of circular polarization (DCP) can be observed in the thermal radio emission at frequencies <100 MHz from the solar corona, due to the difference in the absorption coefficients of the ordinary ("o") and extraordinary ("e") modes of propagation in the magnetized coronal medium. Measurements of this DCP from observations are, however, rare. In this study, we report Stokes-*I* and Stokes-*V* observations of thermal radio emission from the "quiet" solar corona in the frequency range 50–80 MHz, using a one-dimensional radio interferometric polarimeter. The estimated DCP in the above frequency range is ≈2.5%–1.2%. The results indicate the potential in ground-based low-frequency radio observations to estimate the coronal magnetic field in the "quiet" corona in the heliocentric distance range ($r < 2.0\,R_\odot$), where solar radio emission in the above frequency range typically originates.

Unified Astronomy Thesaurus concepts: Quiet solar corona (1992); Solar coronal radio emission (1993); Solar magnetic fields (1503); Solar radio telescopes (1523); Spectropolarimetry (1973)

1. Introduction

The propagation of radio waves through the coronal plasma is profoundly influenced by the magnetic field. The medium becomes anisotropic, and the refractive index becomes a function of the distribution of electron density and magnetic field and the direction of propagation. The radiation will be circularly polarized and propagates in two modes of opposite senses, usually referred to as ordinary ("o") and extraordinary ("e") modes (see, e.g., S. F. Smerd 1950). The radio emission from the "quiet" solar corona at heights $>0.2\,R_\odot$ above the solar surface typically lies at frequencies <100 MHz (where $R_\odot$ is the Sun photospheric radius). At low frequencies, the optical depth is not very large, even for radio emissions from regions near the center of the solar disk (S. F. Smerd 1950; K. V. Sheridan & D. J. McLean 1985; G. Thejappa & M. R. Kundu 1992; C. E. Alissandrakis 1994; R. Ramesh 2005). The observed brightness temperature (T_b) is always less than the electron temperature (T_e) of the corona (see, e.g., G. Thejappa & M. R. Kundu 1992; C. V. Sastry 1994; R. Ramesh et al. 2006; P. Zhang et al. 2022). So, it is possible to detect any change in the optical depth(s) and hence, T_b, due to the presence of a magnetic field. There could be differences in the optical depths between the "o" and "e" modes due to differential absorption, resulting in a detectable degree of circular polarization (DCP; K. Golap & C. V. Sastry 1994; C. V. Sastry 2009).

Gauribidanur Radio Interferometric Polarimeter (GRIP; R. Ramesh et al. 2008)[4] is an one-dimensional interferometric array used for observations of circularly polarized radio emission from the solar corona at frequencies <100 MHz (R. Ramesh et al. 2011, 2013; K. Sasikumar Raja & R. Ramesh 2013; K. Hariharan et al. 2014; K. Sasikumar Raja et al. 2014). Until recently, a 1 bit digital correlator comprising of discrete elements was used in the GRIP to measure interferometric visibilities at two spot frequencies free of radio frequency interference (RFI). The channel bandwidth and integration time were 1 MHz and 0.256 s, respectively. We replaced it with a field-programmable gate array (FPGA)–based system to detect DCP in the thermal emission of the solar corona in the 50–80 MHz frequency range. The new system offers better sensitivity due to direct digitization of the RF signal in the above band (see, e.g., V. Mugundhan et al. 2018). There is continuous coverage of the abovementioned frequency band with 21 channels (channel width ≈1.56 MHz). Data are simultaneously obtained in all the frequency channels with an integration time of ≈10 s. These are important to infer the spectral nature of the observed emission. The above frequency range is chosen because of the possibility to observe circular polarization in thermal radio emission from the solar corona (R. Ramesh & C. V. Sastry 2005; R. Ramesh et al. 2010, 2021; P. I. McCauley et al. 2019). It is well known that the nonthermal radio bursts from the solar corona are brighter at lower frequencies, and hence, they can also be studied. The present configuration of the GRIP is described in Sections 2, 3, and 4. The observations, calibration, analysis, and results are discussed in Section 5.

2. Antennas and Analog Receiver System

The basic receiving antenna element in the GRIP is a log periodic dipole antenna (LPDA), similar to the antennas in the Gauribidanur Radio Heliograph (GRAPH; R. Ramesh et al. 1998). The GRIP has four groups of such LPDAs installed along the east–west direction. The details of the array layout and analog front-end receiver are provided in Table 1 and Figure 1.

[4] https://www.iiap.res.in/centers/gro/

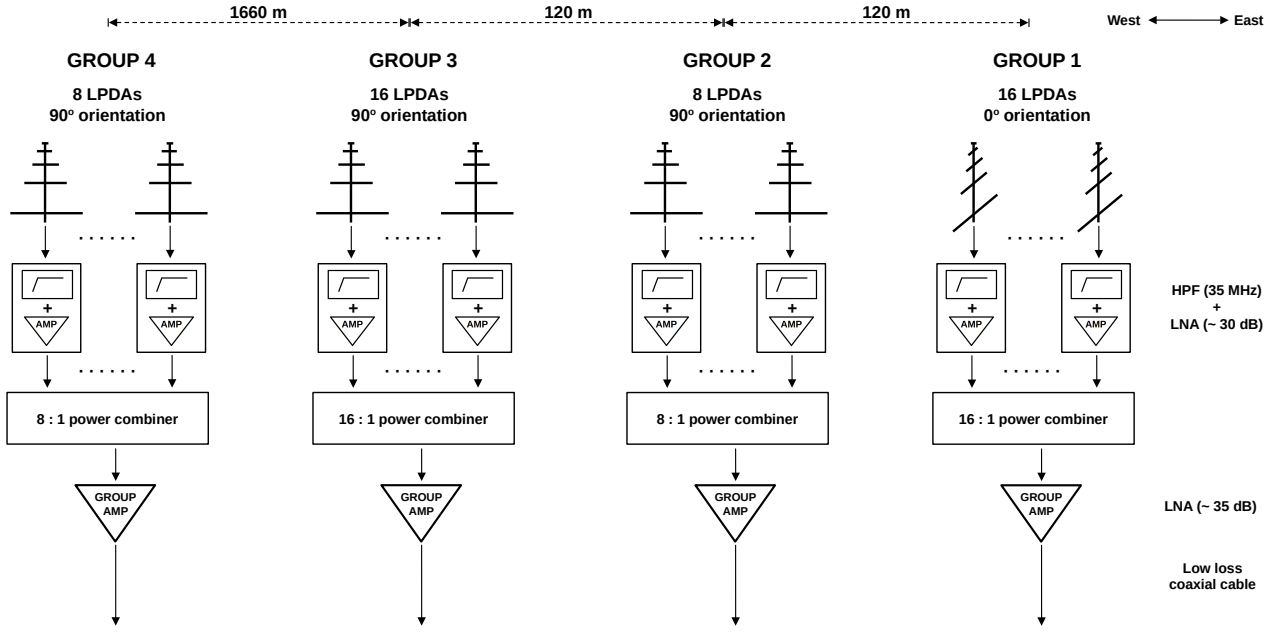

Figure 1. Configuration of the GRIP antenna setup in the field

Table 1
Details of Antenna Groups in GRIP

Name	No. of LPDAs	Orientation of LPDA Arms	Inter-LPDA Spacing (m)	Distance w.r.t. Group-1 Center (m)
Group-1	16	x-direction (0°)	10	0
Group-2	8	y-direction (90°)	10	120
Group-3	16	y-direction (90°)	10	240
Group-4	8	y-direction (90°)	10	1900

Note. Orientation signifies the direction in which the dipoles of the LPDA are aligned. The inter-LPDA spacing signifies the distance between two LPDAs in a group.

The signals received by each antenna are filtered using a 35 MHz high-pass filter (HPF) to remove the low-frequency RFI and amplified by ∼30 dB gain using a low-noise amplifier (LNA). Then, they are transmitted to a location at the centers of the respective groups, where all the antenna signals of that group are combined using a power combiner. The combined group signal is again amplified by ∼35 dB gain and transmitted to the receiver room through low-loss coaxial cables.

The block diagram of the analog signal processing in the receiver room is shown in the upper half of Figure 2. In the receiver room, each group signal is again filtered, amplified, and passed through a 50–80 MHz band pass filter (BPF). Before the 50–80 MHz filter, a radio frequency (RF) attenuator is used to maintain the signal power entering the analog-to-digital converter (ADC) to be within the linear working limits of the ADC.

3. Digital Back-end Receiver System

The digital back-end receiver of GRIP is an FPGA-based system designed to obtain autocorrelation and cross-correlation spectra of the signals from the four antenna groups. We use Reconfigurable Open Architecture Computing Hardware (ROACH), which is a standalone FPGA processing board developed by the Collaboration for Astronomy Signal Processing and Electronics Research (CASPER) and Xilinx.[5] The ROACH has Xilinx Virtex-5 FPGA[6] hardware, and two Atmel/e2V AT84AD001B ADCs[7] are used for digitization. A schematic of the digital receiver system is shown in the lower half of Figure 2. The ADC utilized in the present work is an 8 bit dual-input ADC. It operates in interleaved mode with four output streams per input. An external 800 MHz clock is provided as the clock input to the ADC, such that each of the four output streams of the input signal is sampled at 200 MHz. Only one of the four output streams per input is used for further processing. Overall, two ADCs are used for digitizing the signals from the four groups in the GRIP antenna array, and they convert the voltage signals to an 8 bit fixed-point number between +1 and -1. After digitization, suitable digital delays (in units of the sampling time period) are applied to compensate for the signal chain delay differences between the group signals (Section 2). The geometrical delays experienced by the signal incident on the different antenna groups are not compensated, and hence, there will be interference fringes in the observations of the point sources after cross correlation.

After delay compensation, the voltage spectrum of each group signal is produced using the polyphase filter bank (PFB) technique (D. C. Price 2021). The PFB is a combination of a finite impulse response (FIR) filter and fast Fourier transform (FFT), which produces less interspectral channel leakage than a traditional FFT technique. Our PFB design has a 4 tap FIR filter with a Hamming window and 128 point FFT, which divides the 0–100 MHz band into 64 positive and 64 negative frequency channels of 1.5625 MHz width each (this PFB is

[5] https://casper.astro.berkeley.edu/wiki/ROACH
[6] https://docs.amd.com/v/u/en-US/ds100
[7] https://casper.astro.berkeley.edu/wiki/ADC2x1000-8

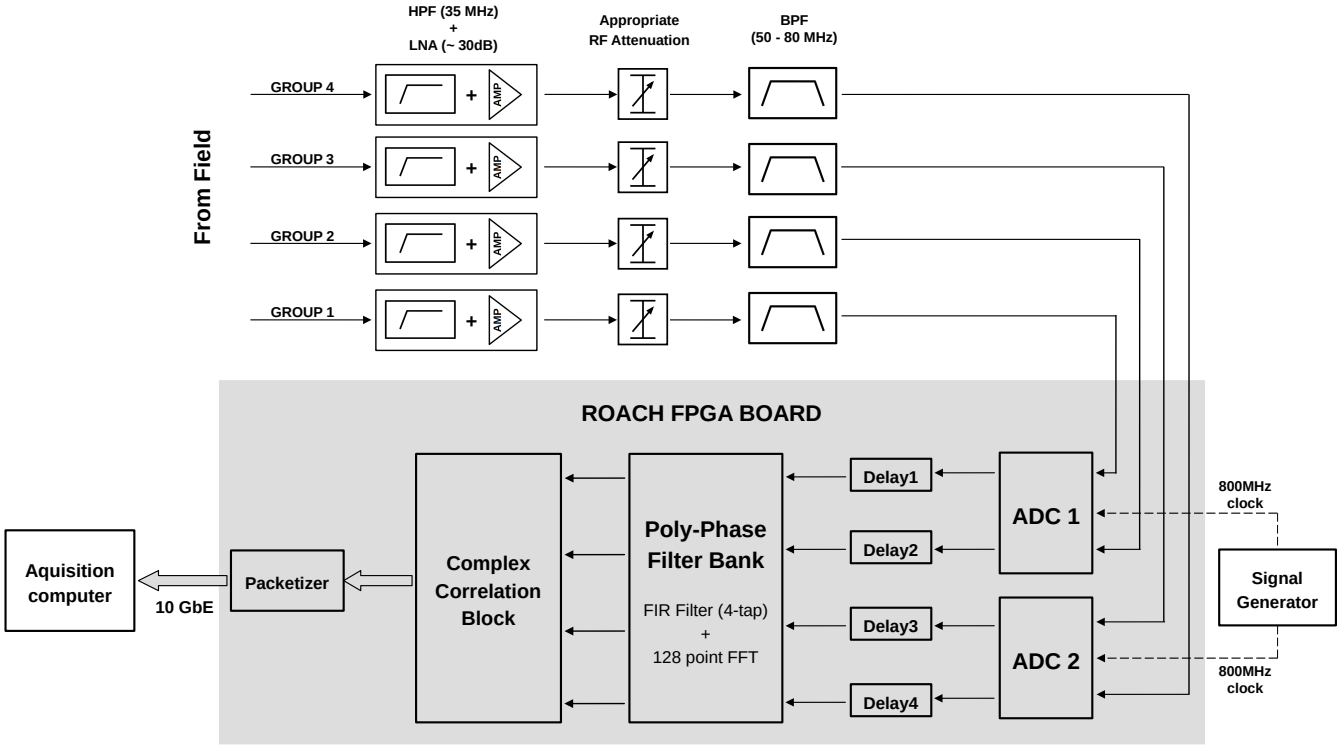

Figure 2. Block diagram of the GRIP back-end receiver system

designed by referring K. S. Bane et al. 2022). Because the information present in the negative frequency channels is the same as that in the positive channels, they are not used for further analysis. Later, in the correlation block, the signals from each antenna group are correlated with one another (complex correlation) at each frequency channel to generate six cross-correlation spectra. In addition, four autocorrelation spectra are also generated. The resultant spectra is recorded on an acquisition computer via a 10 gigabit Ethernet cable in binary format. The acquired data are analyzed using MATLAB/Python programs. Autocorrelation spectral powers are displayed in real time on the acquisition computer to monitor the "health" of the RF signals from the different antenna groups (see, e.g., Figure 3). We routinely maintain the system to ensure that the gain and phase differences between the group signals are at a minimum.

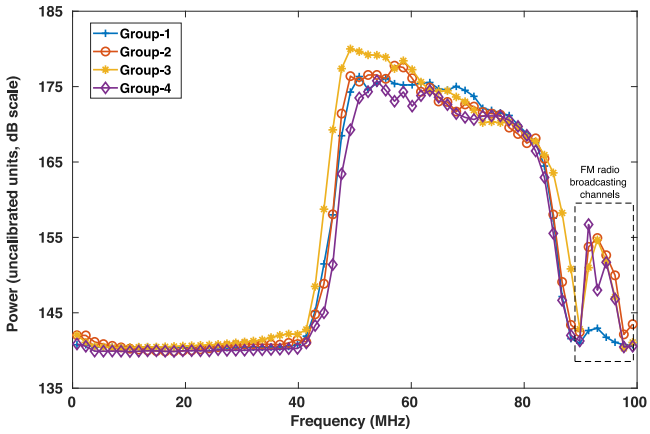

Figure 3. "Raw" autocorrelation profiles of the signals from the four antenna groups in the GRIP at one time instance.

4. Interferometric Visibility Responses of GRIP

The response of an antenna "i" with orthogonally polarized feeds "x" and "y" can be factorized into a number of physically distinct components using the Jones matrix (J_i) as follows (see, e.g., W. D. Cotton 1999):

$$J_i = G_i D_i P_i, \tag{1}$$

where the gain term,

$$G_i = \begin{pmatrix} g_{x_i} & 0 \\ 0 & g_{y_i} \end{pmatrix}, \tag{2}$$

g_{x_i}, and g_{y_i} are the complex gain factors for the signals from the two orthogonal feeds. The leakage term,

$$D_i = \begin{pmatrix} 1 & d_{x_i} \\ -d_{y_i} & 1 \end{pmatrix}, \tag{3}$$

d_{x_i}, and d_{y_i} are the fractions of the orthogonally polarized signal leaking into a given feed. The parallactic rotation term,

$$P_i = \begin{pmatrix} \cos\chi & -\sin\chi \\ \sin\chi & \cos\chi \end{pmatrix}, \tag{4}$$

where χ is the parallactic angle, i.e., the misalignment of the antenna coordinates the frame with respect to (w.r.t.) to the source coordinate frame. For each of the four groups in GRIP system, the Jones matrices can be written as

$$J_1 = \begin{pmatrix} g_{x_1} & 0 \\ 0 & 0 \end{pmatrix}\begin{pmatrix} 1 & d_{x_1} \\ 0 & 1 \end{pmatrix}\begin{pmatrix} \cos\chi & -\sin\chi \\ \sin\chi & \cos\chi \end{pmatrix} \tag{5}$$

$$J_2 = \begin{pmatrix} 0 & 0 \\ 0 & g_{y_2} \end{pmatrix}\begin{pmatrix} 1 & 0 \\ -d_{y_2} & 1 \end{pmatrix}\begin{pmatrix} \cos\chi & -\sin\chi \\ \sin\chi & \cos\chi \end{pmatrix} \tag{6}$$

$$J_3 = \begin{pmatrix} 0 & 0 \\ 0 & g_{y_3} \end{pmatrix} \begin{pmatrix} 1 & 0 \\ -d_{y_3} & 1 \end{pmatrix} \begin{pmatrix} \cos\chi & -\sin\chi \\ \sin\chi & \cos\chi \end{pmatrix} \quad (7)$$

$$J_4 = \begin{pmatrix} 0 & 0 \\ 0 & g_{y_4} \end{pmatrix} \begin{pmatrix} 1 & 0 \\ -d_{y_4} & 1 \end{pmatrix} \begin{pmatrix} \cos\chi & -\sin\chi \\ \sin\chi & \cos\chi \end{pmatrix}. \quad (8)$$

If I, Q, U, and V are the Stokes parameters (fluxes) corresponding to a radio source, then the different possible correlations (C) that can be obtained on an interferometer baseline between the ith and kth antennas with orthogonal polarized feeds can be expressed in Mueller matrix form as follows (see, e.g., W. D. Cotton 1999):

$$\begin{pmatrix} C_{x_i x_k} \\ C_{x_i y_k} \\ C_{y_i x_k} \\ C_{y_i y_k} \end{pmatrix} = (J_i \otimes J_k^*) \frac{1}{2} \begin{pmatrix} 1 & 1 & 0 & 0 \\ 0 & 0 & 1 & j \\ 0 & 0 & 1 & -j \\ 1 & -1 & 0 & 0 \end{pmatrix} \begin{pmatrix} I \\ Q \\ U \\ V \end{pmatrix}, \quad (9)$$

where the operation symbol "$\otimes$" signifies outer matrix product.

The present work focuses on polarization from the "quiet" corona or thermal radio emission in the frequency range 50–80 MHz with a individual channel bandwidth of 1.56 MHz. It is widely reported that linear polarization originating from the solar corona when observed from Earth over a finite bandwidth ($\sim$MHz) will be obliterated because of Faraday rotation in the solar corona and Earth's ionosphere (M. H. Cohen 1958; R. J. M. Grognard & D. J. McLean 1973; A. Boischot & A. Lecacheux 1975; P. I. McCauley et al. 2019). There are few reports of detection of linearly polarized emission from the solar corona at frequencies $<$100 MHz, but they are limited to type III radio burst emission from the "active" Sun and narrow bandwidths of 100 Hz and 10 KHz (R. V. Bhonsle & L. R. McNarry 1964; Y. C. Chin et al. 1971). Unlike the linear polarization, the circular component of polarization is unchanged by the Faraday rotation and depolarization, making it potentially more useful as a probe. Based on the abovementioned observational results, we assume that linear polarized emission, particularly from the "quiet" Sun at frequencies $<$100 MHz and over bandwidths of 1.56 MHz, as in the present case, is expected to be negligible. Therefore, Stokes Q and U, from the source, in Equation (9) can be considered to be $\approx$0 for the current analysis. Further, the GRIP system is equipped to compute $C_{y_i y_k}$ and $C_{y_i x_k}$ correlations only since there are no colocated orthogonal LPDA pairs (i.e., both X- and Y-orientations) in each antenna group (see Sections 2 and 3).

The angular extent of the radio Sun in the frequency range of the GRIP results presented in this work (i.e., 80–50 MHz) is typically in the range $\approx 50' - 38'$ (W. C. Erickson et al. 1977; R. Ramesh et al. 2020; P. Zhang et al. 2022). Therefore, the Sun is a point source for the interferometer baselines between Group-1, Group-2, and Group-3 (we call them short baselines) and is resolved on the baselines with Group-4 (we call them long baselines). In this study, considering commonality, the short baseline multiplications, i.e., Group-3 x Group-2 ($C_{y_3 y_2}$) and Group-2 x Group-1 ($C_{y_2 x_1}$), are used to estimate the DCP of thermal emission from the "quiet" Sun. The total power output, i.e., autocorrelation spectra, from each of the above antenna groups is used to infer the respective channel gains. Differences, if any, are used to calibrate the multiplications involving the respective antenna groups.

Referring to Equation (9), the Mueller matrix for the multiplication between the antenna Group-3 x Group-2 in GRIP is

$$\begin{pmatrix} 0 \\ 0 \\ 0 \\ C_{y_3 y_2} \end{pmatrix} = (J_3 \otimes J_2^*) \frac{1}{2} \begin{pmatrix} 1 & 1 & 0 & 0 \\ 0 & 0 & 1 & j \\ 0 & 0 & 1 & -j \\ 1 & -1 & 0 & 0 \end{pmatrix} \begin{pmatrix} I \\ 0 \\ 0 \\ V \end{pmatrix}. \quad (10)$$

The above matrix multiplication reduces to

$$C_{y_3 y_2} = \frac{1}{2} g_{y_3} g_{y_2}^* I. \quad (11)$$

Similarly, the Mueller matrix for the multiplication between the antenna Group-2 x Group-1 in GRIP is

$$\begin{pmatrix} 0 \\ 0 \\ C_{y_2 x_1} \\ 0 \end{pmatrix} = (J_2 \otimes J_1^*) \frac{1}{2} \begin{pmatrix} 1 & 1 & 0 & 0 \\ 0 & 0 & 1 & j \\ 0 & 0 & 1 & -j \\ 1 & -1 & 0 & 0 \end{pmatrix} \begin{pmatrix} I \\ 0 \\ 0 \\ V \end{pmatrix}. \quad (12)$$

The above matrix multiplication reduces to

$$C_{y_2 x_1} = \frac{1}{2} g_{y_2} g_{x_1}^* ((d_{x_1}^* - d_{y_2}) I - jV). \quad (13)$$

The ratio of Equations (13) and (11) is

$$\frac{C_{y_2 x_1}}{C_{y_3 y_2}} = \frac{g_{x_1}^*}{g_{y_3}} \left((d_{x_1}^* - d_{y_2}) - j \frac{V}{I} \right) \quad (14)$$

$$\frac{V}{I} = j \frac{g_{y_3}}{g_{x_1}^*} \left(\frac{C_{y_2 x_1}}{C_{y_3 y_2}} - \frac{g_{x_1}^*}{g_{y_3}} (d_{x_1}^* - d_{y_2}) \right) \quad (15)$$

$$\left| \frac{V}{I} \right| = \left| \frac{g_{y_3}}{g_{x_1}^*} \right| \left| \left(\frac{C_{y_2 x_1}}{C_{y_3 y_2}} - \frac{g_{x_1}^*}{g_{y_3}} (d_{x_1}^* - d_{y_2}) \right) \right|. \quad (16)$$

5. Observations, Calibration, and Results

The present work utilizes the 2025 July 1 GRIP observations of the Sun (R.A., R.A. = 06^h42^m; decl., $\delta = 23°06'$) as the target source and Taurus-A (R.A. = 05^h34^m; $\delta = 22°00'$) as the calibrator. Both were observed during their respective local meridian transit. The transit time of the Sun at the local meridian is 06:54 UT and of Taurus-A is 05:46 UT (on that day). The difference between the altitude and azimuth of the two sources, when they were observed with GRIP, are $\sim$1° and $\sim$0°, respectively. No long-lived or short-lived nonthermal radio bursts from the Sun were reported during our observations.[8,9] No fringes from the Sun are seen in the long baselines in the observations of Sun, confirming the absence of any point sources of emission in the solar corona. The total intensity image of the Sun at 51 MHz obtained using the GRAPH during the same time also indicate a "quiet" corona (Figure 4). The correlations $C_{y_3 y_2}$ and $C_{y_2 x_1}$ in the majority of the 21 frequency channels in the 50–80 MHz band were analyzed to estimate the DCP in the respective channels, except for a few channels that

[8] https://solarmonitor.org/data/2025/07/01/meta/noaa_events_raw_20250701.txt

[9] https://secchirh.obspm.fr/spip.php?page=survey&hour=day&survey_type=12&dayofyear=20250701

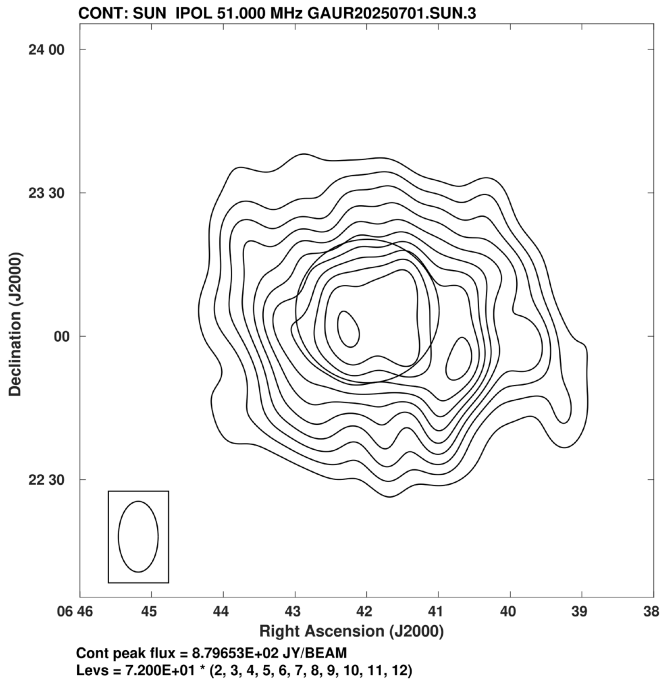

Figure 4. Stokes-*I* image of the solar corona at 51 MHz obtained with the GRAPH on 2025 July 1 around the local meridian transit of the Sun.

were affected by RFI. The analysis and calibration are performed for each individual frequency channel.

5.1. SUN DCP Calibration

As mentioned in Section 5, we used Taurus-A observations to infer the gain and leakage terms in Equation (15). Since the time difference between Taurus-A and Sun observations, during their respective meridian transits, is small (1 hr 8 minutes), we assumed that the time-dependent system properties remain unchanged between the observations of the above two sources. The differences between the altitude and azimuth of the two sources are also small as mentioned in the previous paragraph. So, we directly applied the system parameters determined from Taurus-A observations to Sun observations as correction. Taurus-A can be considered as an unpolarized point source for the GRIP array (see, e.g., R. H. Brown et al. 1955; M. H. Cohen 1958; N. Bucciantini & B. Olmi 2018; F. de Gasperin et al. 2020). So, any noticeable correlation in $C_{y_2x_1}$ (see Equation (13)) can be treated as system leakage from Stokes *I* (see, e.g., E. Lenc et al. 2017). Hence, Equation (14) for Taurus-A can be written as

$$\left(\frac{C_{y_2x_1}}{C_{y_3y_2}}\right)_{tau} = \frac{\boldsymbol{g}^*_{\boldsymbol{x_1}}}{g_{y_3}}(d^*_{x_1} - d_{y_2}). \tag{17}$$

The gain ratio term $\left|\frac{g_{y_3}}{\boldsymbol{g}^*_{\boldsymbol{x_1}}}\right|$ is estimated from the autocorrelation (total power) measurements in the respective channels 1 and 3. From the calculated $\left|\frac{g_{y_3}}{g^*_{x_1}}\right|$ and $\left(\frac{C_{y_2x_1}}{C_{y_3y_2}}\right)_{\rm tau}$, the Sun's DCP (in percentage) can be estimated using Equations (16) and (17) as

Table 2
Uncalibrated DCP Measurements of Sun and System Leakage from Taurus-A at Different Frequencies from GRIP on 2025 July 1

Frequency (MHz)	Uncalibrated Sun's DCP (%)	System leakage from Taurus-A (%)
49.2	10.40	8.003
52.3	11.92	9.381
53.9	14.13	11.80
55.4	8.447	6.081
57.0	4.590	2.440
61.7	6.777	4.969
66.4	6.510	5.109
74.2	5.893	4.707
78.9	7.654	6.481
80.4	7.988	6.757

the following:

$$\begin{aligned}\mathrm{DCP}_{\rm sun} &= \left|\frac{V}{I}\right| \times 100 = \left|\frac{g_{y_3}}{g^*_{x_1}}\right| \left|\left(\frac{C_{y_2x_1}}{C_{y_3y_2}}\right)_{\rm sun} - \left(\frac{C_{y_2x_1}}{C_{y_3y_2}}\right)_{\rm tau}\right| \times 100 \\ &= \left|\left(\frac{g_{y_3}}{g^*_{x_1}}\right)\left(\frac{C_{y_2x_1}}{C_{y_3y_2}}\right)_{\rm sun} - \left(\frac{g_{y_3}}{g^*_{y_1}}\right)\left(\frac{C_{y_2x_1}}{C_{y_3y_2}}\right)_{\rm tau}\right| \times 100.\end{aligned} \tag{18}$$

In the present work, we have considered only the magnitude of the DCP (Equation (18)). So, there will not be any reduction in DCP due to possible system-induced phase difference (e.g., cross-hand phase) between signals from the orthogonal group $\boldsymbol{y_3}$ and $\boldsymbol{x_1}$. The $\boldsymbol{C_{y_{2x_1}}}$ correlation holds both the Stokes-*V* and Stokes-*U* visibilities (Equation (9)). As Stokes *U* is negligible in our case, any leakage of Stokes *V* to Stokes *U* (due to cross-hand phase) will not change/reduce the magnitude of the $\boldsymbol{C_{y_{2x_1}}}$ correlation. It will only alter the phase. Also, the reduction in DCP due to the nonorthogonality between *X*- and *Y*-oriented antennas (e.g., ellipticity error) is minimum in GRIP antennas. Table 2 shows the uncalibrated DCP obtained using Sun observations and the system leakage obtained using Taurus-A observations, at different frequencies of GRIP. In Equation (18), the first and second terms correspond to the Sun's uncalibrated DCP and system leakage, respectively. From Table 2, it can be seen that the Sun's DCP is larger than the leakage in the system, indicating there is circularly polarized emission from the Sun, over and above the leakage. Figure 5 shows the corrected Sun's DCP (i.e., after subtracting the leakage; see, e.g., R. I. Reid et al. 2008; E. Lenc et al. 2018). In Figure 6, we have shown the system leakages estimated from GRIP observations of the brightest A-team sources in the northern sky (F. de Gasperin et al. 2020) at a typical GRIP observing frequency (52 MHz) and the corresponding values derived using the WIPL-D software package[10] (v21, WIPL-D 2024) by designing the structure of the LPDA antenna used in the GRIP. There is a good agreement between the observations and simulations, indicating the WIPL-D simulated values can be effectively used to correct for the leakage DCP in Sun observations when it is observed at other declinations in the range -23°S to +23°N also.

[10] https://wipl-d.com/products/wipl-d-pro-cad/

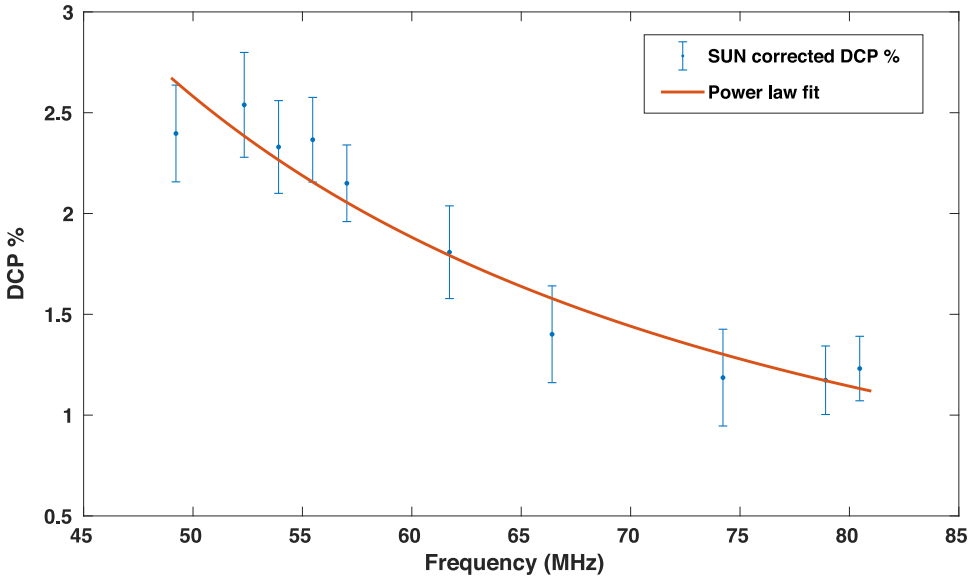

Figure 5. Estimated Sun DCP after calibration using GRIP on 2025 July 1. The power-law fit (red line) to the data points shows a clear decrease in DCP with increase in frequency. The error bars in the DCP estimations correspond to the 1σ noise fluctuations in the observations.

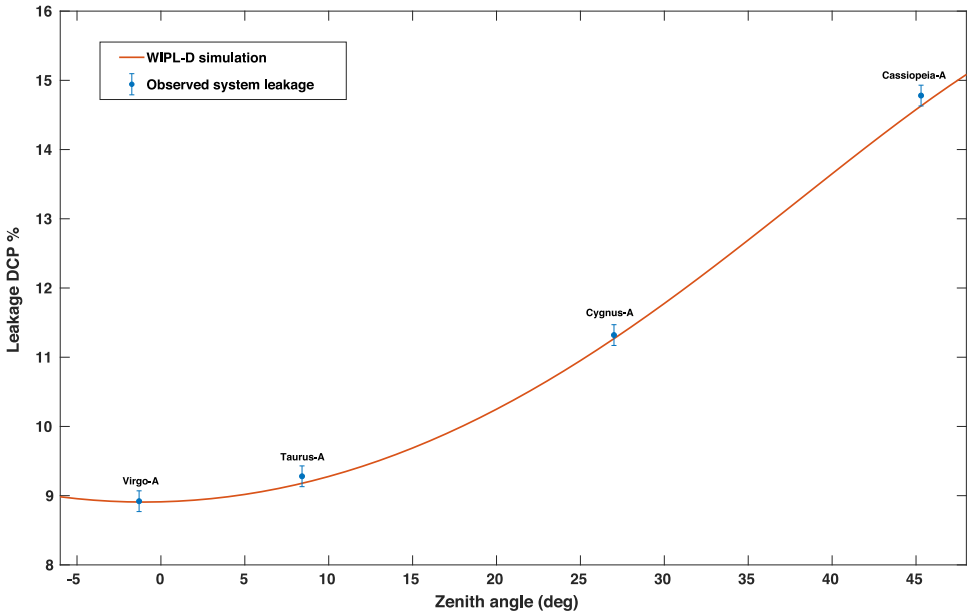

Figure 6. System leakage estimated from GRIP observations of the A-team sources at 52 MHz and the corresponding values derived using WIPL-D software by designing the structure of the LPDA antenna used in the GRIP.

5.2. Sun Flux Calibration

From Equation (11), the interferometric responses for the Sun and Taurus-A observations can be written as

$$(C_{y_3y_2})_{\text{tau}} = \frac{1}{2}(g_{y_3}g^*_{y_2})I_{\text{tau}} \tag{19}$$

$$(C_{y_3y_2})_{\text{sun}} = \frac{1}{2}(g_{y_3}g^*_{y_2})I_{\text{sun}}. \tag{20}$$

From Equations (19) and (20), and assuming $g_{y_3}g^*_{y_2}$ remains unchanged between observations of the Sun and Taurus-A (Section 5.1), the calibrated Stokes-I flux from Sun can be given as

$$I_{\text{sun}} = \left| \frac{(C_{y_3y_2})_{\text{sun}}}{(C_{y_3y_2})_{\text{tau}}} \right| I_{\text{tau}}. \tag{21}$$

Likewise, the calibrated Stokes-V flux from Sun after correcting the DCP (Section 5.1) is

$$V_{\text{sun}} = \left(\frac{\text{DCP}_{\text{sun}}}{100}\right) \times I_{\text{sun}}. \tag{22}$$

The calibrated Stokes-I and -V profiles at a few frequencies are shown in Figure 7. The estimated Stokes-I flux densities as a function of frequency are shown in Figure 8. Using power-law fit to the data points in Figure 8, we estimated the spectral

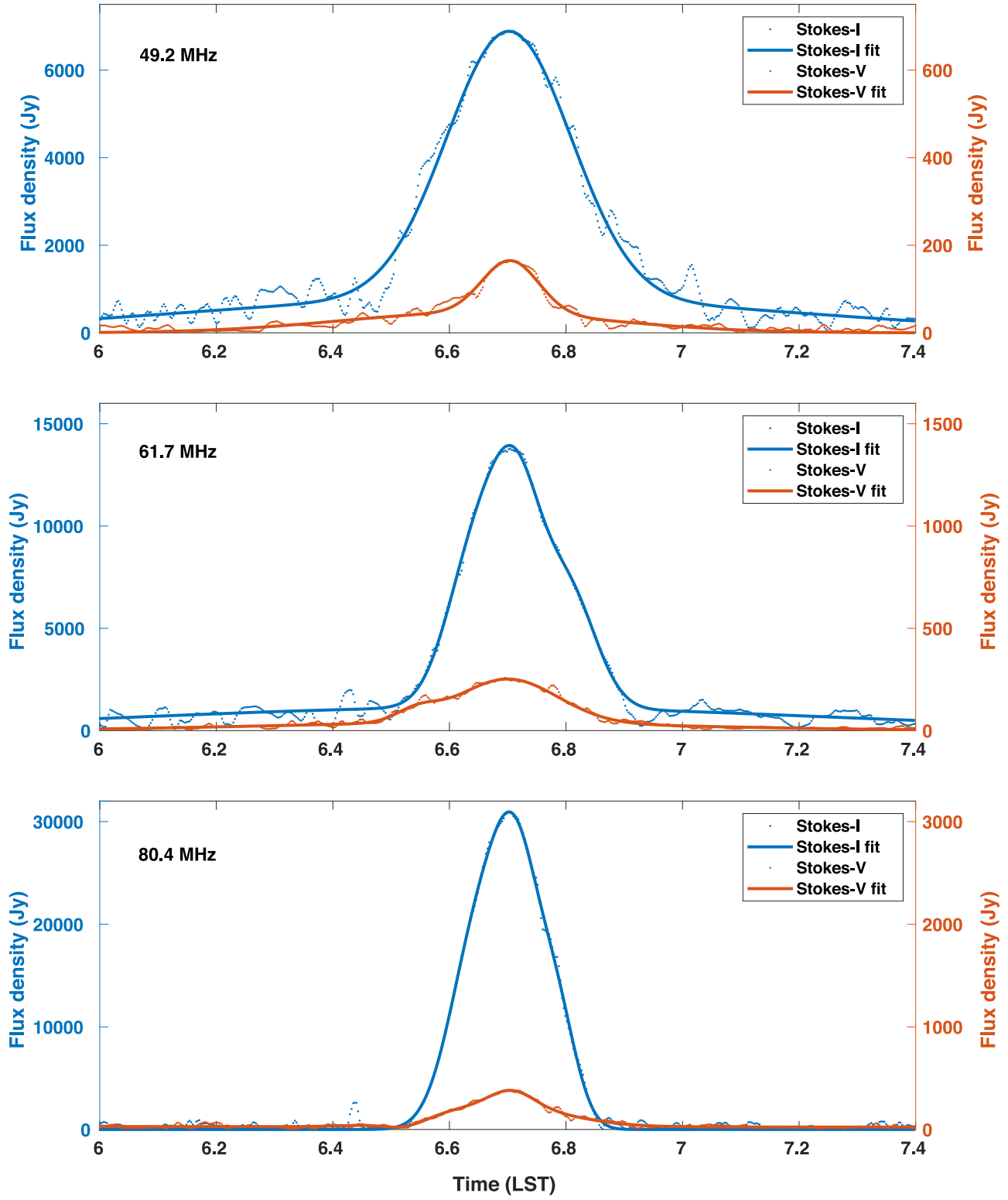

Figure 7. Stokes-*I* and -*V* observations in a few frequency channels in the GRIP on 2025 July 1 around the local meridian transit of the Sun. Blue and orange colors indicate Stokes *I* and Stokes *V*, respectively. Their flux densities are shown separately in the left-side and right-side *y*-axes. The dots represent the data points, and the continuous line profiles are their least-square fits.

index of Stokes-*I* emission as $\approx 2.9 \pm 0.3$. This value is in the range of spectral indices reported by different authors for thermal emission from the "quiet" solar corona at frequencies < 100 MHz (W. C. Erickson et al. 1977; K. R. Subramanian & C. V. Sastry 1988; R. Ramesh et al. 2006; C. Vocks et al. 2018; P. Zhang et al. 2022). The decrease in DCP with increase in frequency (lower panel in Figure 5) is consistent with the reported calculations for circularly polarized thermal radio emission from the "quiet" solar corona (C. V. Sastry 2009) and is likely due to comparatively larger optical depths at higher

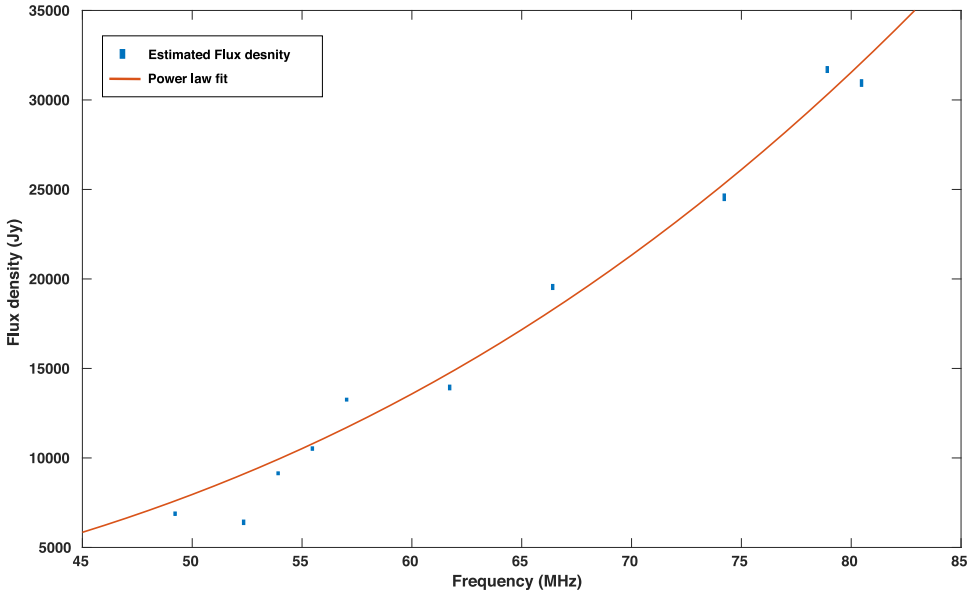

Figure 8. Calibrated Stokes-*I* flux densities of SUN estimated at different frequencies from GRIP observations on 2025 July 1 around local meridian transit of the Sun. The red line is the power-law fit to the data points. The height of the blue rectangular data points shows the error bar of the estimated flux density value.

frequencies (Section 1). In such a situation, any difference between the optical depths of the ordinary and extraordinary modes, which is linked to the Stokes-*V* flux, is expected to be less pronounced.

6. Summary

We have presented low-frequency (50–80 MHz) observations of thermal radio emission from the "quiet" solar corona in Stokes *I* and Stokes *V* with the GRIP system. The estimated DCP values are consistent with the results reported using ray-tracing calculations. Currently, one of the most reliable methods for measuring the magnetic field in the corona is through its influence on the radio emission (see, e.g., C. E. Alissandrakis & D. E. Gary 2021). With several interesting results related to the measurements of the solar coronal magnetic field often reported from low-frequency radio observations of nonthermal emission from the solar radio bursts, the results described in this work indicate the potential in the radio observations at frequencies <100 MHz to obtain two-dimensional images of the distribution of the field strengths in the "quiet" corona also. Observations with large antenna arrays that operate at frequencies <100 MHz are expected to be very useful in achieving this. The GRAPH array, which routinely observes the solar corona every day and generates two-dimensional Stokes-*I* images at spot frequencies <100 MHz, is currently being upgraded to simultaneously observe and generate images in Stokes-*V* emission. Observations during solar eclipses in the above frequency range is another possibility since data could be obtained at higher angular resolution (see, e.g., R. Ramesh et al. 1999; C. Kathiravan et al. 2011; A. M. Ryan et al. 2021).

Acknowledgments

We are grateful to the Gauribidanur Observatory team for their help in the observations and upkeep of the facilities. We thank the observatory team members Shanmukh, Rajesh, Santosh and Nagendra for their contributions in the upgradation of GRIP array. We also thank the reviewer for insightful comments that helped to present the results more clearly.

Software: Matlab, WIPL-D.

ORCID iDs

Shaik Sayuf https://orcid.org/0000-0003-4598-6830
C. Kathiravan https://orcid.org/0000-0002-6126-8962
R. Ramesh https://orcid.org/0000-0003-2651-0204
Indrajit V. Barve https://orcid.org/0000-0002-1030-9082
G. V. S. Gireesh https://orcid.org/0000-0003-0741-0144
Kshitij S. Bane https://orcid.org/0000-0002-8550-9070

References

Alissandrakis, C. E. 1994, AdSpR, 14, 81
Alissandrakis, C. E., & Gary, D. E. 2021, FrASS, 7, 77
Bane, K. S., Barve, I. V., Gireesh, G. V. S., Kathiravan, C., & Ramesh, R. 2022, JATIS, 8, 017001
Bhonsle, R. V., & McNarry, L. R. 1964, ApJ, 139, 1312
Boischot, A., & Lecacheux, A. 1975, A&A, 40, 55
Brown, R. H., Palmer, H. P., & Thompson, A. R. 1955, MNRAS, 115, 487
Bucciantini, N., & Olmi, B. 2018, MNRAS, 475, 822
Chin, Y. C., Lusignan, B. B., & Fung, P. C. W. 1971, SoPh, 16, 135
Cohen, M. H. 1958, PIRE, 46, 172
Cotton, W. D. 1999, ASPC, 180, 111
de Gasperin, F., Vink, J., McKean, J. P., et al. 2020, A&A, 635, A150
Erickson, W. C., Gergely, T. E., Kundu, M. R., & Mahoney, M. J. 1977, SoPh, 54, 57
Golap, K., & Sastry, C. V. 1994, SoPh, 150, 295
Grognard, R. J. M., & McLean, D. J. 1973, SoPh, 29, 149
Hariharan, K., Ramesh, R., Kishore, P., Kathiravan, C., & Gopalswamy, N. 2014, ApJ, 795, 14
Kathiravan, C., Ramesh, R., Barve, I. V., & Rajalingam, M. 2011, ApJ, 730, 91
Lenc, E., Anderson, C. S., Barry, N., et al. 2017, PASA, 34, e040
Lenc, E., Murphy, T., Lynch, C. R., Kaplan, D. L., & Zhang, S. N. 2018, MNRAS, 478, 2835
McCauley, P. I., Cairns, I. H., White, S. M., et al. 2019, SoPh, 294, 106
Mugundhan, V., Ramesh, R., Kathiravan, C., Gireesh, G., & Hegde, A. 2018, SoPh, 293, 41
Price, D. C. 2021, in The WSPC Handbook of Astronomical Instrumentation, ed. A. Wolszczan, Vol. 1 (World Scientific), 159
Ramesh, R. 2005, IAUS, 226, 83
Ramesh, R., Kathiravan, C., & Narayanan, A. S. 2011, ApJ, 734, 39

Ramesh, R., Kathiravan, C., & Sastry, C. V. 2010, ApJ, 711, 1029
Ramesh, R., Kathiravan, C., SundaraRajan, M. S., Barve, I. V., & Sastry, V. 2008, SoPh, 253, 319
Ramesh, R., Kumari, A., Kathiravan, C., Ketaki, D., & Wang, T. J. 2021, GeoRL, 48, e91048
Ramesh, R., Kumari, A., Kathiravan, C., et al. 2020, GeoRL, 47, e90426
Ramesh, R., Nataraj, H. S., Kathiravan, C., & Sastry, C. V. 2006, ApJ, 648, 707
Ramesh, R., Sasikumar Raja, K., Kathiravan, C., & Satya Narayanan, A. 2013, ApJ, 762, 89
Ramesh, R., & Sastry, C. V. 2005, ASPC, 346, 153
Ramesh, R., Subramanian, K. R., & Sastry, V. 1999, SoPh, 185, 77
Ramesh, R., Subramanian, K. R., SundaraRajan, M. S., & Sastry, C. V. 1998, SoPh, 181, 439
Reid, R. I., Gray, A. D., Landecker, T. L., & Willis, A. G. 2008, RaSc, 43, RS2008
Ryan, A. M., Gallagher, P. T., Carley, E. P., et al. 2021, A&A, 648, A43
Sasikumar Raja, K., & Ramesh, R. 2013, ApJ, 775, 38
Sasikumar Raja, K., Ramesh, R., Hariharan, K., Kathiravan, C., & Wang, T. J. 2014, ApJ, 796, 56
Sastry, C. V. 1994, SoPh, 150, 285
Sastry, C. V. 2009, ApJ, 697, 1934
Sheridan, K. V., & McLean, D. J. 1985, in Solar Radiophysics: Studies of Emission from the Sun at Metre Wavelengths, ed. D. J. McLean & N. Labrum (Cambridge Univ. Press), 443
Smerd, S. F. 1950, AuSRA, 3, 34
Subramanian, K. R., & Sastry, C. V. 1988, JApA, 9, 225
Thejappa, G., & Kundu, M. R. 1992, SoPh, 140, 19
Vocks, C., Mann, G., Brietling, F., et al. 2018, A&A, 614, A54
Zhang, P., Zucca, P., Kozarev, K., et al. 2022, ApJ, 932, 17